

## PECULIARITIES OF COPPER PRECIPITATION IN HYPEREUTECTOID STEELS

N. V. Stepanova,<sup>1</sup> R. I. Mikhalev,<sup>2</sup> and T. D. Tarasova<sup>3</sup>

UDC 669.017.16

Two series of steel samples with a copper content of 0–9 wt.% were obtained. The first series is a hypereutectoid steel with varying copper content. The structure of the samples of the second series contains graphite formed as a result of modification inside the mold with 0.15 wt.% of silicocalcium. The paper shows the change in the form of graphite with an increase in the copper content in steel. Particular attention was paid to the structure of the particles of the  $\epsilon$ -Cu phase. The study presents a scheme for the formation of a structure inside large particles of the  $\epsilon$ -Cu phase. By reducing the solubility of iron in copper inside the  $\epsilon$ -Cu phase during crystallization and cooling of the particles of the  $\epsilon$ -Cu phase, the formation of three types of particles based on iron is anticipated. The results of the influence of copper on the following mechanical properties are shown: hardness, ultimate strength under uniaxial static tension and compression.

**Keywords:** hypereutectoid steel, structure,  $\epsilon$ -Cu structure, graphite, cementite, mechanical properties.

### Introduction

Copper-alloyed antifriction iron-carbon alloys, such as cast irons and graphitized steels, are used for manufacturing parts of sliding friction units in large mechanisms, since an increased copper content in iron-carbon alloys decreases the coefficient of sliding friction, which contributes to an increase in wear resistance of such alloys [1–15]. However, it is well-known that due to an extremely low solubility of copper in iron at room temperature, almost all copper precipitates as a  $\epsilon$ -Cu phase [7–10]. At a temperature above 1,094 °C, this phase is in a liquid state [12, 14, and 15]. The deformation of a material containing liquid inclusions leads to its fracturing. For this reason, medium and low carbon steels that are not used in as-cast state, and after the pressure treatment may contain no more than 2–3% of copper (this is the maximum percentage of copper that can be dissolved in the iron matrix at temperatures typical for material processing) [8]. Therefore, cast iron-carbon alloys, containing more than 2–3% of copper, which can be used in as-cast state or after a heat treatment, most often include hypereutectoid steels and cast iron, or graphitized eutectoid steels, especially if these are alloys containing more than 6 wt.% of copper [8]. Due to a narrow specialization of these materials (i.e., they are mostly used in large sliding friction units), the number of studies dedicated to iron-carbon alloys with high copper content, produced by casting, is quite limited. Some of such studies address the effect of copper on the antifriction and mechanical properties of iron-carbon alloys [1–15], as well as on corrosion resistance [19–24]. Most of them deal with alloys containing less than 2% of copper. Clearly, there are commonly known antifriction materials based on iron, carbon, and copper, obtained by powder metallurgy methods [25–27]. However, it is not appropriate to compare the structure of such materials with that of the materials obtained by casting methods, since the sintering temperature is usually 60–90% of the melting point of the powder of the single-component system, or lower than

<sup>1</sup> Novosibirsk State Technical University, Novosibirsk, Russia; e-mail: stepanova@corp.nstu.ru.

<sup>2</sup> Novosibirsk State Technical University, Novosibirsk, Russia; e-mail: mixalev.2017@stud.nstu.ru.

<sup>3</sup> Novosibirsk State Technical University, Novosibirsk, Russia; e-mail: t.tarasova.tx121@ya.ru.

**Table 1**  
**Elemental Composition of Finished Castings**

Marking	Concentration, wt.%								
	C	Mn	Si	P	S	Ni	Cr	Cu	Al
ZS0.1Cu								0.09	
GZS0.1Cu								0.1	
ZS3Cu								3	
GZS2.97Cu								2.97	
ZS6.02Cu	2.1	0.36	0.29	0.01	0.01	0.03	0.04	6.02	1.2
GZS6.03Cu								6.03	
ZS8.97Cu								8.97	
GZS8.86Cu								8.76	

the melting point of the base material, if there are several powders [28, 29]. Such materials are widely used in various vehicle assemblies and mechanisms of the sewing equipment. However, their use in large-sized heavy-loaded sliding friction units is limited by high cost and relatively low tensile strength. For example, grade PA-ZhGrD5a material (GOST 26802–86) has a tensile strength of 150 MPa. The use of such materials is limited to relatively small-sized products operating at high speeds. Their *PV* criterion does not exceed  $20 \cdot \text{kG} \cdot \text{m}/\text{cm}^2$  [27].

The *Purpose of This Study* is to develop cast antifriction materials based on iron-carbon alloy with high copper content for use in large-sized heavy-loaded sliding friction units. The studies described in this paper are mostly fundamental. Currently, the structural specifics of cast alloys with high copper content (in particular, the process of formation of the  $\epsilon$ -Cu phase in the particle structure, as well as its interaction with and impact on other structural components, such as graphite) have not been sufficiently studied. This research is aimed at establishing the effect of copper on the process of graphite formation in steel, at analyzing the structure and mechanism of formation of the  $\epsilon$ -Cu particle structure, as well as at the interaction of this phase with cementite and graphite.

## Materials and Procedures

A melt of hypereutectoid steel containing 0–9 wt.% was obtained in an induction furnace (OKB-281) using a crucible with a capacity of 750 kg. The samples were cast into sand-liquid-glass molds weighing 20 kg. Materials marked as GZ were modified by a silicocalcium compound (GOST 4762–71). This compound was used to form graphite in the steel structure. The modification was performed inside the mold, and the modifier content was 0.15 wt.%. The chemical analysis of the materials obtained during the experiments was performed by using an optical emission spectrometer (ARL-3460). The results of the casting sample analysis are shown in Table 1. The lower sulfur and phosphorus contents were achieved by using steel and graphite-containing

material as furnace charge, and by adding aluminum as a reducing agent and alloying element to the melt at the end of melting.

The structure of the samples was analyzed using the equipment provided by the Resource sharing center “Structure, Mechanical and Physical Properties of Materials,” such as the Carl Zeiss Axio Observer A1m optical microscope, Carl Zeiss EVO 50 XVP scanning electron microscope, equipped with the EDSX-Act microanalyzer, and FEI Technai G2 TWIN transmission electron microscope. The phase analysis of the resulting alloys was performed using an X-ray  $\theta$ - $\theta$  diffractometer (ARL X'TRA). A copper X-ray tube was used as the source of X-ray radiation (voltage — 40 kV, current — 40 mA). Materials were analyzed in the geometry of reflected radiation.

The hardness of all samples was determined by the Brinell method. The microhardness of the individual phases of all samples was evaluated by the Vickers method using a microhardness tester (*Wolpert Group 402 MVD*) at a diamond indenter load of 1 N. The material strength was evaluated using the *Instron 300 DX* universal servohydraulic tester based on two schemes: uniaxial static tension and uniaxial static compression of the samples.

## Results and Discussion

During the experiment, two series of samples containing ~0–9 wt.% of copper were obtained. The structure of the samples of the first batch (marked as ZS) contained cementite, while the structure of the samples of the second batch (marked as GZS) contained graphite formed instead of cementite (marking is shown in Table 1). The reason for the graphite formation is the modification of the samples with 0.15 wt.% of the SiCa compound. Similar to the previously conducted studies concerning the effect of copper on the structure and properties of cast iron [9, 10], an increase in pearlite dispersion was observed at higher copper content in the composition of hypereutectoid and graphitized hypereutectoid steels. According to the TEM-based analysis, an increase in the copper content to ~3% leads to a change in the inter-plate distance from 65 to 0.4  $\mu\text{m}$ . Further increase in copper content does not significantly affect the inter-plate distance and thickness of the cementite plates.

***The Effect of Copper on the Form and Distribution of Graphite.*** Based on the structural analysis methods, it was established that the introduction of copper into graphitized (samples marked as “GZS”) hypereutectoid steel is accompanied by a change in the morphology of graphite inclusions. Compact graphite dominated in the alloy containing the minimum percentage of copper (0.1% Cu) (Fig. 1(a)). An increase in copper content of steel leads to a change in the form of graphite from compact to vermicular (see Fig. 1). The first changes in the form of graphite inclusions were observed upon introduction of 2.97 wt.% of copper into steel. In particular, some graphite inclusions demonstrated branching from the base plate (see Fig. 1(b)).

As the copper content increases to 5.03%, changes in the form of graphite inclusions become more apparent. Based on Fig. 1(c), it can be concluded that graphite inclusions are evenly distributed throughout the steel structure, while almost all of them have multiple branches. In the alloy containing 8.76% of copper, vermicular graphite was found in the interdendritic space in the form of a mesh composed of individual plates (see Fig. 1(d)). By analyzing the images of the microstructure of graphitized hypereutectoid steel containing 8.76% of copper using the ImageJ software product, it was shown that the average size of mesh-forming graphite plates was ~5  $\mu\text{m}$  (graphite plate mesh is shown as *l* in Fig. 1(d)).

***Specifics of  $\epsilon$ -Cu Phase Precipitation.*** It is practical to analyze structural transformations during crystallization of hypereutectoid and graphitized hypereutectoid steels by using a polythermal cross-section of the Fe–C–Cu phase diagram, when the carbon content is as close as possible to that of the studied alloys (2%) (Fig. 2).

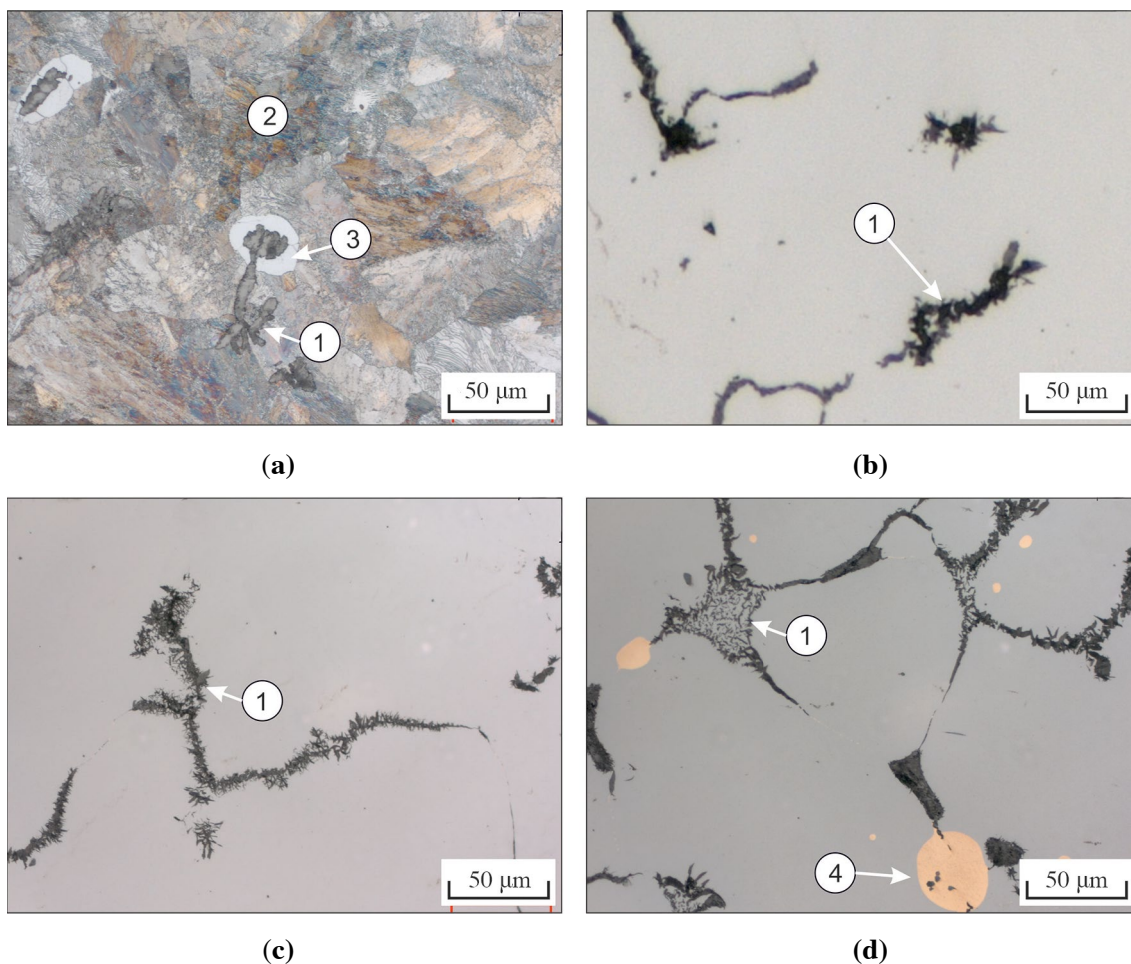


**Fig. 1.** Effect of copper on the form and distribution of graphite in doped hypereutectoid steel: (a) 0.1% Cu; (b) 2.97% Cu; (c) 5.03% Cu; (d) 8.76% Cu; 1 — graphite, 2 — pearlite, 3 — ferrite, 4 — copper inclusions.

The authors of this study used the results of thermodynamic calculations performed in Ref. [17] along with the FactSage software to calculate the isopleth cross-section of the Fe–Cu–C phase diagram, corresponding to 2 wt.% carbon content and 0–40 wt.% copper content. The results of performed calculations are shown in Fig. 2.

In the initial state, hypereutectoid steel (samples marked as “ZS”) contains micro-volumes of lamellar pearlite and inclusion of secondary cementite (~9%), precipitated in the form of a mesh along the boundaries of the former austenite grains.

A specific feature typical for pearlite in steels alloyed with ~3% of copper is the presence of a multitude of finely dispersed inclusions of the  $\epsilon$ -Cu phase, precipitated from the ferritic matrix as a result of a change in the solubility of copper in  $\alpha$ -Fe during cooling. The average size of such inclusions was ~20–30 nm.

In the alloy containing ~6% Cu, two types of copper-based inclusions were observed. The nano-sized particles were located in the ferritic spaces of pearlite, while the larger particles were located along the boundaries of the former  $\gamma$ -Fe grains. The coarser particle formation was caused by a reduction in solubility of copper in  $\gamma$ -Fe upon cooling of the alloy. Such particles are formed in the temperature range from ~1,250 to 727°C. It should be noted that the temperature of 1,250°C corresponds to the maximum content of copper in austenite (6%). The average size of the large particles of  $\epsilon$ -Cu is 1–2  $\mu$ m. According to statistical studies, the average

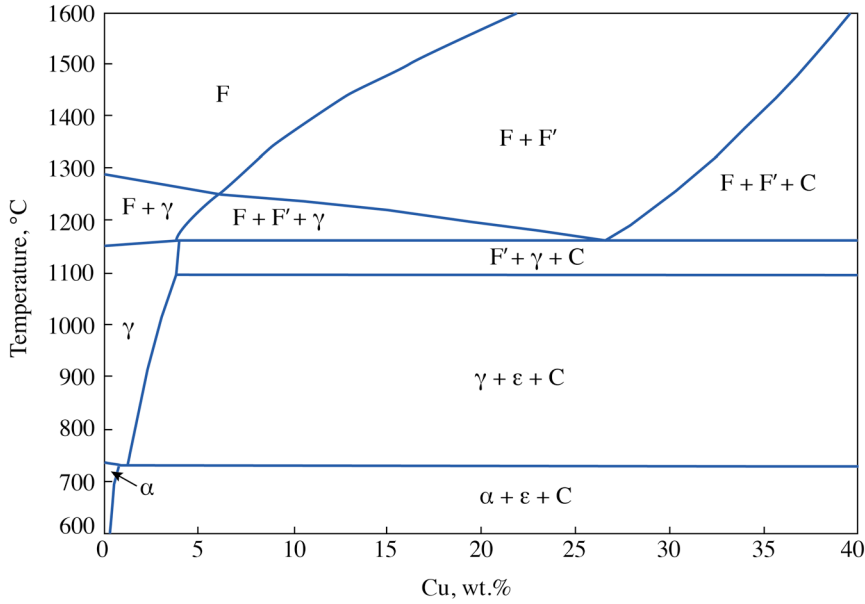


**Fig. 2.** Isopleth (polythermal) cross-section of the Fe–Cu–C diagram with 2 wt.% carbon: F – iron-rich liquid; F' – copper-rich liquid; C – graphite;  $\gamma$  – FCC iron-based solid solution;  $\alpha$  – BCC iron-based solid solution;  $\epsilon$  – FCC copper-based solid solution.

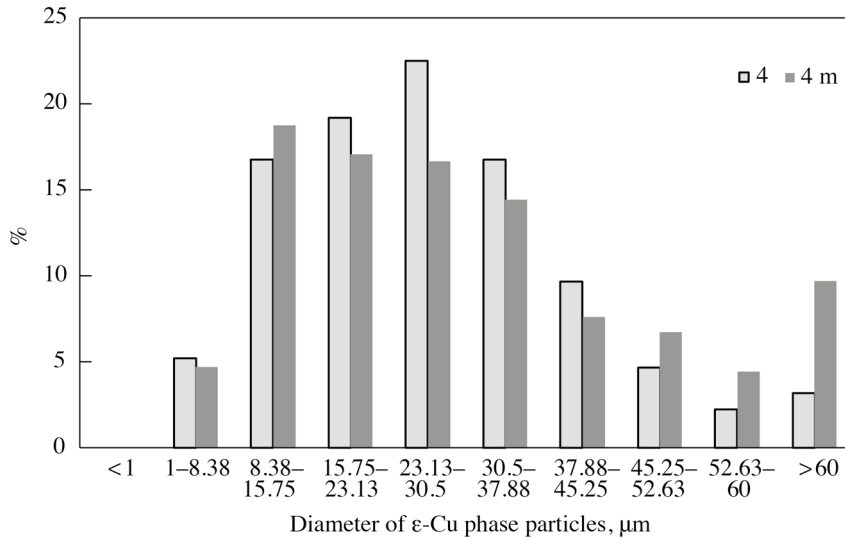


**Fig. 3.** Particle size distribution of  $\epsilon$ -Cu phase in hypereutectoid steel doped with 8.97% Cu and graphitized hypereutectoid steel containing 8.76% Cu.

size of inclusions of this type in the alloy containing 8.97% of copper is  $\sim 25 \mu\text{m}$ . The nature of the  $\epsilon$ -phase particle distribution, plotted based on the results of optical metallography of steel containing 8.97% Cu, can be characterized by using Fig. 3. This distribution has already been published earlier [29], but in this study, it is compared with the results obtained for graphitized hypereutectoid steels.

No copper-based inclusions were detected by optical microscopy in graphitized hypereutectoid steel (samples marked as “GZS”), containing less than 6% Cu. Particles of  $\epsilon$ -Cu phase with an average size of 1–2  $\mu\text{m}$

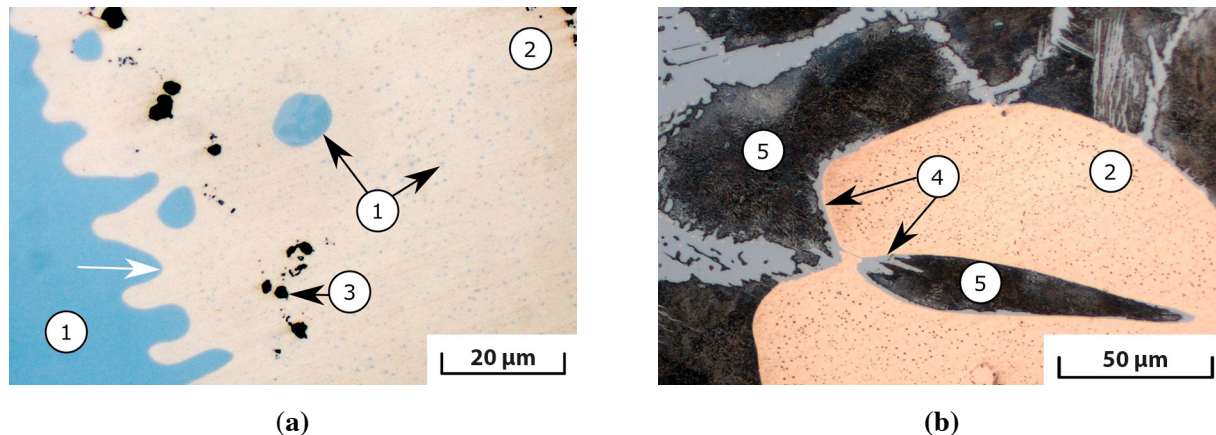


**Fig. 4.** Structure of large-sized  $\epsilon$ -Cu phase particles of hypereutectoid steel: (a) non-etched structure; (b) after etching with 5%  $\text{HNO}_3$ . The white arrow shows the boundary of a large-sized  $\epsilon$ -Cu particle; 1 — Fe-rich particles within the  $\epsilon$ -Cu phase; 2 —  $\epsilon$ -Cu; 3 — graphite; 4 — secondary cementite; 5 — perlite.

were observed in the alloy containing 6.03% of copper. Further increase in copper content was accompanied by an increase in the number and size of inclusions. Their distribution in the casting containing 8.76% Cu is shown in Fig. 3.

The diagram shows two peaks that correspond to  $\epsilon$ -Cu inclusions, measuring  $\sim 20$  and  $\sim 70$   $\mu\text{m}$ , respectively. It can be assumed that they were formed during cooling of the casting according to different mechanisms and at different temperatures. Note that only one peak is observed in the case of non-graphitized steel (see Fig. 3). The microstructure images were analyzed by using the ImageJ software product. When plotting each distribution, the sample size was at least 10,000 measurements.

**Structural Specifics of the Large-Sized  $\epsilon$ -Cu Phase Particles.** Special attention during this study was paid to the structure of the largest  $\epsilon$ -Cu particles. Some large-sized  $\epsilon$ -Cu particles have uneven boundaries. Separate fragments of the iron-carbon alloy structure can be located next to the boundary and inside the  $\epsilon$ -Cu particle (Fig. 4(a)).

An image of the  $\epsilon$ -Cu particle, containing a large fragment of the iron-carbon alloy structure, is shown in Fig. 4(b). The copper-rich liquid has captured the iron-rich liquid. In the process of crystallization, austenite was crystallized inside a still liquid  $\epsilon$ -Cu particle. Later, secondary cementite was formed along the austenite —  $\epsilon$ -Cu interface. A growth of secondary cementite also occurred along the outer boundary of the  $\epsilon$ -Cu particle.

If the crystallization rate was lower, allowing graphite to be formed (when considering samples of graphitized hypereutectoid steel), then graphite inclusions may be located at the boundary as well as inside the  $\epsilon$ -Cu particle (more often, near the boundary) (Fig. 5). It is likely that the concentration of carbon was increasing in the process of austenite crystal growth in the remaining iron-rich liquid. This substance was pushed towards the boundaries similar to the copper-rich liquid, and at 1,153°C, the excess amount of carbon from this substance started forming graphite crystals. Since the copper-based phase remained in the liquid state at these temperatures, graphite inclusion was developing from the austenite —  $\epsilon$ -Cu interface towards the liquid phase. Perhaps due to convection, thin graphite plates inside the liquid  $\epsilon$ -Cu phase were breaking off and repositioned inside the inclusion (see Fig. 5(a)).

It is worth noting that according to the data reported in Ref. [27], the solubility of carbon in liquid copper is 0.001 wt.% at 1,100°C, while the data reported in Ref. [31–34] provide values lower by two orders of magnitude. It is also known that carbon does not diffuse into solid copper [26]. Therefore, graphite inclusions could



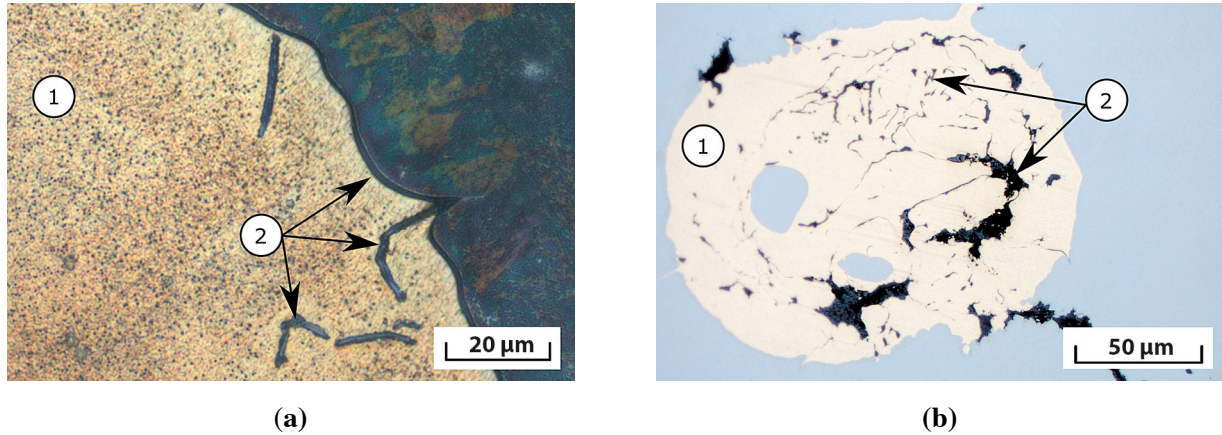


**Fig. 5.** Particles of the  $\epsilon$ -Cu phase with graphite inclusions inside: 1 —  $\epsilon$ -Cu; 2 — graphite.

not have been formed inside the  $\epsilon$ -Cu phase and likely made it inside from the surface. Thus, it is possible to sometimes observe the  $\epsilon$ -Cu phase with graphite inclusions located inside of it (see Fig. 5(a)). Quite often graphite inclusions are located near the surface of the  $\epsilon$ -Cu particle (see Fig. 5).

When analyzing the iron-rich corner of the Fe–Cu–C phase diagram with 2% carbon content (see Fig. 2), it can be seen that due to the change in copper solubility in iron, the  $\epsilon$ -Cu inclusions have different sizes, depending on the formation phase and  $\epsilon$ -Cu phase precipitation temperature. Previously, a  $\epsilon$ -Cu particle formation scheme was presented based on the analysis of the iron-rich corner of the Fe–Cu–C diagram with 3 wt.% carbon content [9]. Four types of such particles have been identified, and their characteristics, such as size distribution and preferential formation site, were described. It should be noted that the smallest particles are formed from  $\alpha$ -Fe below the pearlite transformation temperature and have a size of  $\sim 20$  nm in case of crystallization of the cast samples [10]. Similar particles are also detected at high cooling rates, for example, when obtaining material under non-vacuum electron beam welding [36].

In this study, special attention was paid to the internal structure of the largest  $\epsilon$ -Cu particles. The microhardness of this structural component is  $\sim 160$  HV. According to an EDX analysis performed using scanning electron microscopy, in addition to copper, these particles also contain  $\sim 3$ –4% of iron and  $\sim 2$ % of aluminum. The most copper-rich alloy in this study contains only  $\sim 9$ % Cu. In this case, the structure of large-sized copper-based particles is quite complex (see Fig. 4). These particles were formed from the melt and were still in the liquid state when the entire iron-based phase had already crystallized. As follows from the analysis of the crystallization process of these structural areas (these particles), they crystallized according to the copper-rich corner of the Fe–Cu–C diagram as a copper-based alloy, containing 4% of iron. The schematic of the crystallization process of such particles is shown in Fig. 6. The analysis was performed by utilizing a section of the Fe–Cu–C phase diagram with 5 wt.% carbon content [13].

Upon cooling, a stratification of iron-based and copper-based liquids takes place. As a result, large-sized iron-based particles (irregularly shaped) “float” in the pool of copper-based liquid. Such particles in the  $\epsilon$ -Cu phase structure are shown in Fig. 7(a). An EDX analysis using scanning electron microscopy was used to perform scanning along the line of such micro-volumes to show that these areas contain iron (see Fig. 7(b)). According to the optical metallographic analysis, these areas have an average size of  $\sim 20$   $\mu\text{m}$  and a structure of pearlite (see Fig. 7(a)).

Next, the formation of a  $\gamma$ -Fe solid phase in the copper-based liquid takes place, since above  $1,094^\circ\text{C}$ , the  $\epsilon$ -Cu phase is in the liquid state, while the  $\gamma$ -Fe phase is solid. In this case, the iron-based phase particles are

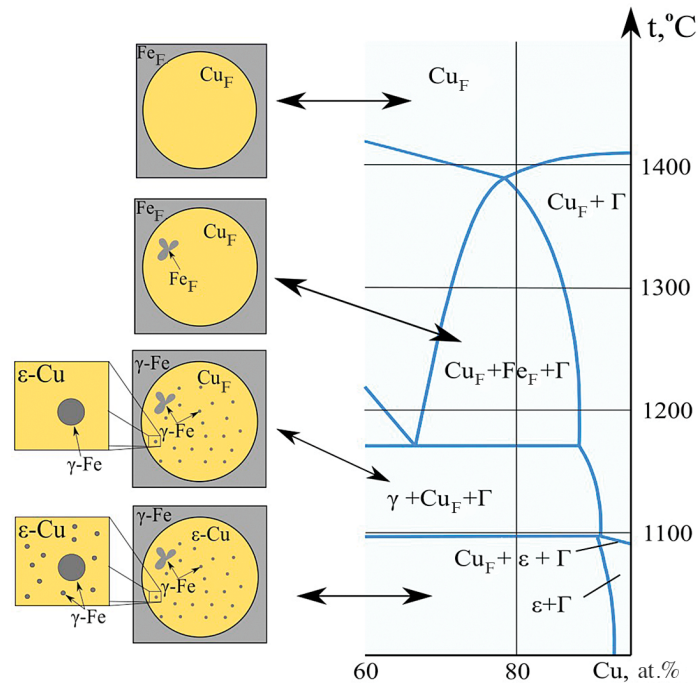


**Fig. 6.** Schematic of the crystallization process inside large-sized  $\epsilon$ -Cu phase particles.

formed, which are uniformly distributed inside the large-sized particles of the  $\epsilon$ -Cu phase and have a near-spherical shape. Such shape is likely due to the fact that the  $\gamma$ -Fe particles were in the liquid, and did not experience any limitations. When studying the structure using optical metallographic methods, uniformly distributed particles having a near-spherical shape (see Fig. 4 and Fig. 7(a)) and an average size of  $\sim 0.4$ – $0.5$   $\mu\text{m}$  (Fig. 8) were detected inside the large-sized  $\epsilon$ -Cu phase particles. When analyzing the etched structure of the  $\epsilon$ -Cu phase sections using SEM methods, particles having an average size of  $0.5$   $\mu\text{m}$  were also observed (marked as 1 in Fig. 7(b)), which likely represent the  $\alpha$ -Fe phase.

As can be seen from the diagram shown in Fig. 6, the  $\epsilon$ -Cu phase is in the solid state at temperatures below  $1,094^\circ\text{C}$ . In addition, as the temperature decreases, so does the solubility of copper in iron. Another important factor is the decrease in the iron diffusion rate in the solid  $\epsilon$ -Cu phase upon cooling [36]. As a consequence, such conditions should lead to the formation of iron-based particles having the smallest size. In this study, no TEM analysis of the structure of the large-sized  $\epsilon$ -Cu particles was performed. However, when studying the iron-doped copper-based alloys, the authors of Ref. [37] have shown that  $\alpha$ -Fe particles having an average size of  $\sim 20$ – $50$  nm are formed in the  $\epsilon$ -Cu phase. In addition, as can be seen in Fig. 7(b), there is a graphite inclusion located inside the  $\epsilon$ -Cu phase, which has grown into it when this phase was still in a liquid state. This is also confirmed by the shape of the  $\epsilon$ -Cu — pearlite interface. A structure of the base material shown in Fig. 7(d) is characterized by the presence of multiple inclusions of the  $\epsilon$ -Cu particles with an average size of  $\sim 20$  nm, which are uniformly distributed within the ferritic spaces of pearlite. This is typical for all alloys in this study with a copper content in excess of 3 wt.%.

The XRD patterns of hypereutectoid steels doped with 0.08 and 3.01% of copper indicate the presence of solid solution based on  $\alpha$ -Fe and cementite (Fig. 9). As the copper content reaches 3.01%, there is a slight increase in the volumetric fraction of  $\text{Fe}_3\text{C}$ . Also, with a copper content of 3.01% and higher, an increase in the width of the main  $\alpha$ -Fe peak at half-height by  $\sim 15\%$  (0.05 deg.) can be seen (see Fig. 2). In hypereutectoid steel alloyed with 6.02% of copper, there is 2.8% of the  $\epsilon$ -Cu phase in addition to ferrite and cementite.



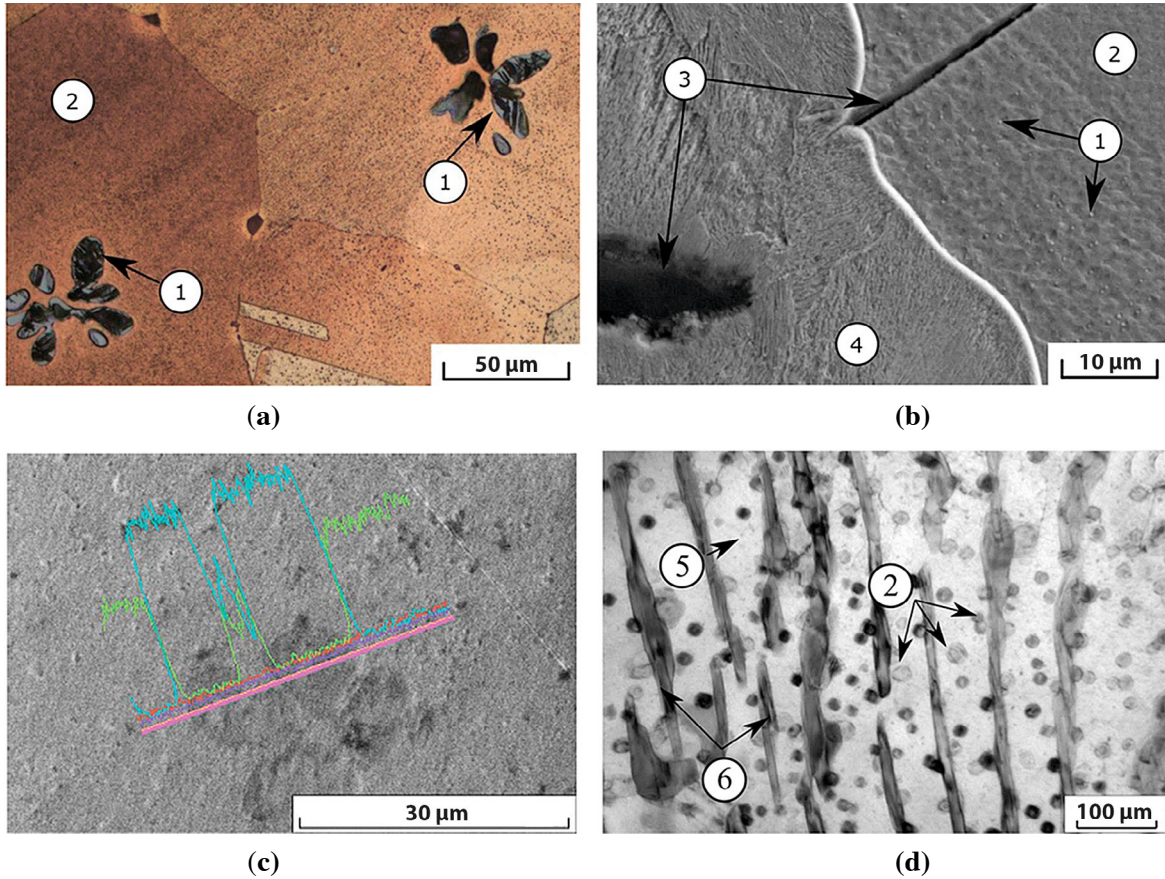


**Fig. 7.** Structural specifics of the ZS8.97Cu sample: (a) iron-based inclusions inside the  $\epsilon$ -Cu particle; (b) SEM; (c) results of scanning along the iron-based particle line inside the large-sized  $\epsilon$ -Cu particle, where the blue graph corresponds to iron, and green graph — to copper; (d) TEM of the main material of the ZS8.97Cu sample; 1 — Fe-rich particles within the  $\epsilon$ -Cu phase; 2 —  $\epsilon$ -Cu; 3 — graphite; 4 — pearlite; 5 —  $\alpha$ -Fe; 6 —  $\text{Fe}_3\text{C}$ .

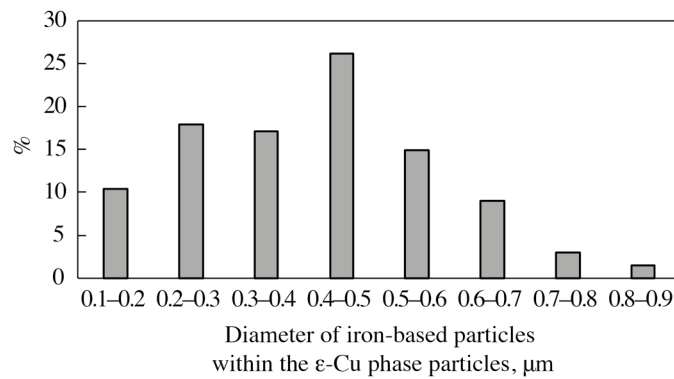


**Fig. 8.** Particle distribution within the  $\epsilon$ -Cu phase.

When the copper content is 8.97 wt.%, the volumetric fraction of the  $\epsilon$ -Cu phase (according to XRD analysis) reaches 5.4% (see Fig. 9). No intermetallic compounds of the Al-Fe system were found. Based on the results of an EDX analysis performed using scanning electron microscopy, the distribution of aluminum in all materials is uniform. According to the Fe-Cu-Al diagram [38], only  $\alpha$ -Fe and  $\epsilon$ -Cu phases can be detected

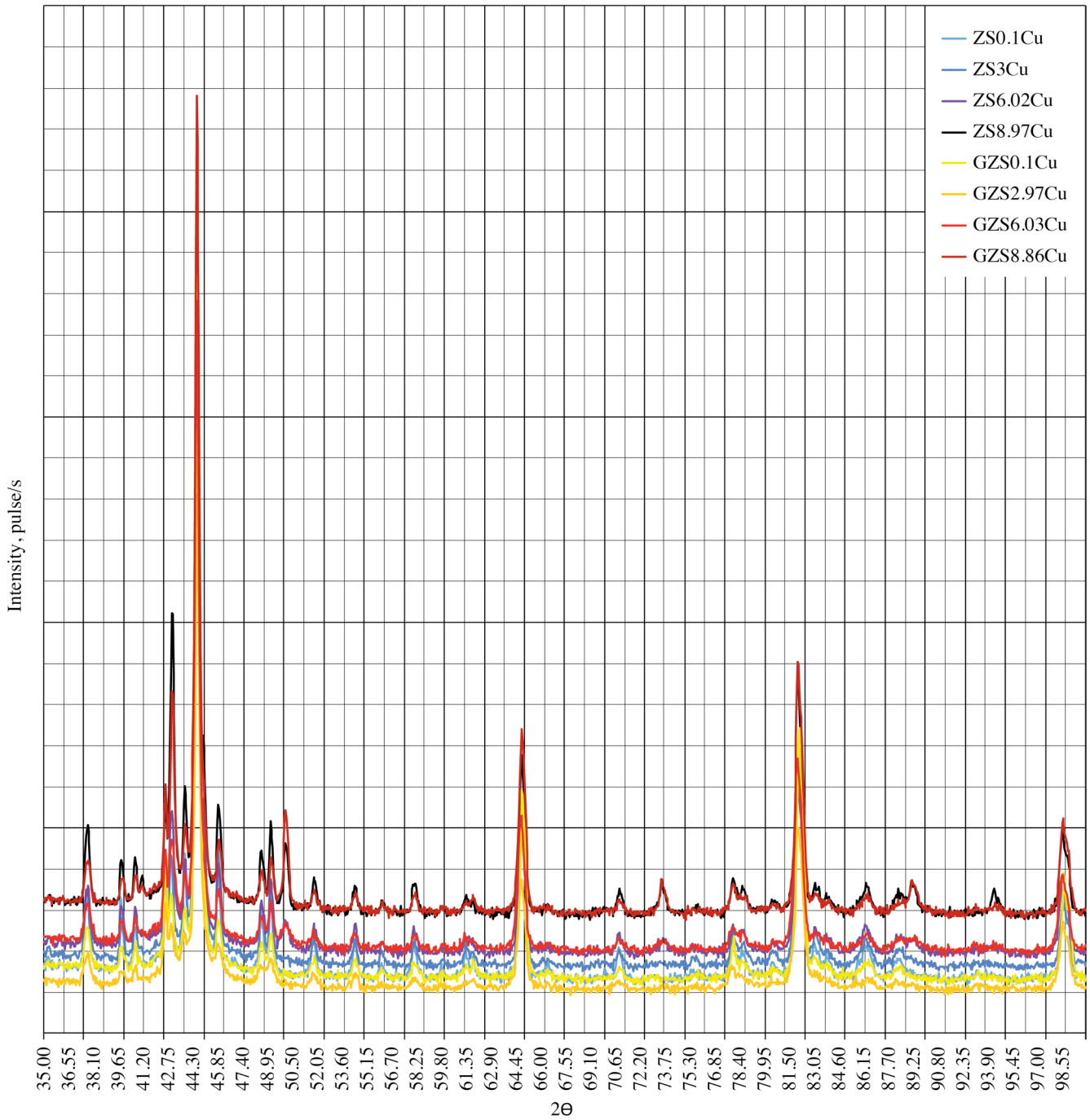


**Fig. 9.** Results of XRD analysis of copper-doped hypereutectoid steels.

in the composition at 600°C, when the aluminum content is ~1–2%. The Fe<sub>3</sub>C phase can also be detected due to the presence of carbon in the composition of the studied materials. The X-ray patterns of the graphitized hypereutectoid steels do not have any fundamental differences compared to those shown in Fig. 9. Since their volumetric fraction of graphite is small, the graphite peak is located at the noise level, and therefore cannot be clearly detected.

***The Effect of Copper on the Mechanical Properties of Hypereutectoid and Graphitized Hypereutectoid Steels.*** One specific feature typical for the alloys studied in the paper is that their hardness level increases with the copper content. The doping effect is most noticeable when the copper content is increased to ~3 wt.%. The hardness of non-graphitized hypereutectoid steel varies from 340 to 390 HB. An increase in the hardness of graphitized hypereutectoid steel is expressed to a lesser extent (from 250 to 280 HB). Based on the analysis of the test results obtained in the study, it becomes possible to conclude that the hardness of the tested alloys increases when the copper content reaches ~6–7 wt.%, however, the rate of such increase is lower compared to the 0–3% range. An increase in the level of hardness observed in this study can be explained by a number of factors. The effect of these factors is demonstrated by an increase in the microhardness of pearlite as the main structural component of all studied alloys. The main reasons for the increase in the microhardness of lamellar pearlite are associated with an increase in dispersion of the ferrite-cementite mixture, precipitation of strengthening nano-sized copper particles in the ferritic spaces of the colonies, as well as the presence of dissolved copper atoms in  $\alpha$ -Fe. Doping of the studied alloys with copper has resulted in an increase in the microhardness of pearlite from 350 to 430 HV in graphitized hypereutectoid steel, and from 390 to 460 HV in hypereutectoid steel.

For hypereutectoid steels, doping with copper typically results in an increase in strength characteristics. For example, by introducing 9% of Cu into hypereutectoid steel, it becomes possible to increase its tensile strength from 300 to 430 MPa. In graphitized hypereutectoid steel of a similar composition, an increase in tensile strength due to the introduction of copper is less by 50 MPa.

When introducing 9% of copper, the compression strength of non-graphitized hypereutectoid steel varies from 1,550 to 1,700 MPa. For graphitized hypereutectoid steel, the analyzed range is from 1,050 to 1,200 MPa. The reason for lower strength values of graphitized steel has to do with the properties of graphite, the inclusions of which can be viewed as irregularly shaped pores, causing the concentration of mechanical stresses. The presence of graphite inclusions affects both tensile and compression strengths under the uniaxial static testing.

## CONCLUSIONS

1. During in-mold modification of hypereutectoid steel with 0.15 wt.% of SiCa, graphite precipitation occurs in the steel structure. An introduction of copper into graphitized hypereutectoid steel leads to a gradual change in the morphology of graphite from a compact form to a vermicular type, located in an interdendritic space, with mesh-forming plates having an average size of ~5  $\mu\text{m}$ .

2. Structural specifics of the  $\epsilon$ -Cu phase and graphite formation have been established. Graphite can be formed on the surface of a liquid particle of the  $\epsilon$ -Cu phase and can be located inside the particle near the interface.

3. A schematic of structure formation inside large-sized  $\epsilon$ -Cu phase particles is presented. During crystallization and cooling of the  $\epsilon$ -Cu phase particles, the formation of three types of iron-based particles is anticipated due to a reduction in the solubility of iron in copper inside the  $\epsilon$ -Cu phase. The largest particles have an irregular shape and a size of ~20  $\mu\text{m}$ . At the time of their formation, these particles are in a liquid state and can be found inside a copper-based liquid. The medium-sized particles have a spherical shape and a size of ~0.5  $\mu\text{m}$ . At the time of their formation, they represent  $\gamma$ -Fe crystals located in a copper-based liquid phase. The smallest particles should have a size of ~20 nm and be formed as a result of a change in the solubility of iron in  $\epsilon$ -Cu [38].

4. With an increase in copper content to 3 wt.%, the hardness of both hypereutectoid and graphitized hypereutectoid steels increases by 50 and 30 HB, respectively. Further increase in copper content also results

in the hardness growth, but the latter is less pronounced. The data correlate well with an increase in pearlite microhardness. The main reasons for the increase in the microhardness of lamellar pearlite are associated with an increase in dispersion of ferrite-cementite mixture and precipitation of strengthening nano-sized copper particles in the ferritic spaces of the colonies.

5. An introduction of 9% of Cu to hypereutectoid steel leads to an increase in its tensile and compression strength from 300 to 430 MPa and from 1,550 to 1,700 MPa, respectively. In graphitized hypereutectoid steel of a similar composition, an increase in tensile strength due to the introduction of copper is less by 50 MPa, while the compression strength changes from 1,050 to 1,200 MPa. The reason for the lower strength values in graphitized steels has to do with the presence of graphite in their structure.

### Acknowledgement

Special thanks to Dr. Youn-Bae Kang of the Graduate Institute of Ferrous Technology, Pohang University of Science and Technology, Pohang 790–784, Republic of Korea for developing an isopleth (polythermal) section of the Fe–Cu–C diagram with 2 wt.% carbon content.

The studies were performed using the equipment provided by the Resource sharing center “Structure, Mechanical and Physical Properties of Materials” (agreements No. 13.TsKP.21.0034 and 075-15-2021-698 of the Ministry of Education and Science). The study was sponsored by the NSTU development program, research project No. C22-14.

### REFERENCES

1. W. Osterle, C. Prietzel, H. Kloss, and A. I. Dmitriev, “On the role of copper in brake friction materials,” *Tribology Intern.*, **43**, 2317–2326 (2010).
2. J. O. Agunsoye, S. A. Bello, S. B. Hassan, R. G. Adeyemo, and J. M. Odii, “The effect of copper addition on the mechanical and wear properties of grey cast iron,” *J. of Minerals and Materials Characterization and Engineering*, **2**, 470–483 (2014).
3. B. Zhang, B. Xu, and Yi Xu, “Cu nanoparticles effect on the tribological properties of hydrosilicate powders as lubricant additive for steel-steel contacts,” *Tribology Intern.*, **44**(7), 878–886 (2011).
4. W. Zhai, W. Lu, and X. Liu, “Nanodiamond as an effective additive in oil to dramatically reduce friction and wear for fretting steel/copper interfaces,” *Tribology Intern.*, **129**, 75–81 (2019).
5. A. C. P. Rodrigues, W. Oesterle, and T. Gradt, “Impact of copper nanoparticles on tribofilm formation determined by pinon-disc tests with powder supply: Addition of artificial third body consisting of Fe<sub>3</sub>O<sub>4</sub>, Cu and graphite,” *Tribology International*, **110**, 103–112 (2017).
6. M. Eroglu, “Boride coatings on steel using shielded metal ARC welding electrode: microstructure and hardness,” *Surface & Coatings Technology*, **203**, 2229–2235 (2009).
7. G. I. Silman, V. V. Kamynin, and V. V. Goncharov, “On the mechanisms of copper effect on the formation of cast iron structure,” *Metallovedeniye i Termicheskaya Obrabotka Metallov (MiTOM)*, No. 9, 16–22 (2007).
8. *Copper in Iron and Steel*, ed. by I. Le May and L. M. -D. Schetky [in Russian], transl. from English (ed. by O. A. Bannykh), Metallurgiya, Moscow (1988).
9. A. A. Bataev, N. V. Stepanova, I. A. Bataev, Y. Kang, and A. A. Razumakov, “Special features of precipitation of ε-Cu phase in cast irons alloyed with copper and aluminum,” *Metal Science and Heat Treatment*, **60**(3–4), 150–157 (2018).
10. N. V. Stepanova, I. A. Bataev, Y. Kang, D. V. Lazurenko, A. A. Bataev, A. A. Razumakov, A. M. Jorge Jr., “Composites of copper and cast iron fabricated via the liquid: In the vicinity of the limits of strength in a non-deformed condition,” *Materials Characterization*, **130**, 260–269 (2017).
11. S. Upadhyay and K. K. Saxena, “Effect of Cu and Mo addition on mechanical properties and microstructure of grey cast iron: An overview,” *Materials Today-Proc.*, **26**, 2462–2470 (2020).
12. H. Sazegaran, F. Teimoori, H. Rastegarian, and A. M. Naserian-Nik, “Effects of aluminum and copper on the graphite morphology, microstructure, and compressive properties of ductile iron,” *J. of Mining and Metallurgy, Section B: Metallurgy*, **57**, 1, 145–154 (2021).

13. L. N. Garcia, A. J. Tolley, F. D. Carazo, and R. E. Boeri, "Identification of Cu-rich precipitates in pearlitic spheroidal graphite cast irons," *Materials Science and Technology*, **35**, 18, 2252–2258 (2019).
14. A. Vaško, Ju. Belan, and E. Tillová, "Effect of copper and molybdenum on microstructure and fatigue properties of nodular cast irons," *Manufacturing Technology*, **18**, 6, 1049–1052 (2018).
15. "Effect of graphene on friction and wear behavior of friction composite tested against grey cast iron disc alloyed with copper," *Carbon Trends*, **3** (2021); DOI 10.1016/j.cartre.2021.100031.
16. G. I. Sil'man, V. V. Kamynin, and A. A. Tarasov, "Effect of copper on structure formation in cast iron," *Metal Science and Heat Treatment*, **45**, 7–8, 254–258 (2003).
17. K. Shubhank and Y. Kang, "Critical evaluation and thermodynamic optimization of Fe–Cu, Cu–C, Fe–C binary systems and Fe–Cu–C ternary system," *Computer Coupling of Phase Diagrams and Thermochemistry*, **45**, 127–137 (2014).
18. G. I. Sil'man, "About retrograde solidus and stratification of melt in the Fe–Cu and Fe–Cu–C systems," *Metal Science and Heat Treatment*, **51**, 1–2, 19–24 (2009).
19. D. M. Buck, "Copper in steel — the influence on corrosion," *J. of Industrial and Engineering Chemistry*, **5** (6), 447–452 (1913).
20. B. Li, H. Qu, and Y. Lang, "Copper alloying content effect on pitting resistance of modified 00Cr20Ni18Mo6CuN super austenitic stainless steels," *Corrosion Science*, **173**, Art. 108791 (2020).
21. X. Y. Sun, B. Zhang, B. Wu, X. X. Wei, E. E. Oguzie, and X. L. Ma, "Investigating the effect of Cu-rich phase on the corrosion behavior of Super 304H austenitic stainless steel by TEM," *Corrosion Science*, **130**, 143–152 (2018); <http://doi.org/10.31788/RJC.2021.1456678>.
22. Z. X. Zhang, G. Lin, and Z. Xu, "Effects of light pre-deformation on pitting corrosion resistance of copper-bearing ferrite antibacterial stainless steel," *J. of Materials Processing Technology*, **205**, 419–424 (2008).
23. S. Jeon, S. Kim, I. Lee, J. Park, K. Kim, J. Kim, and Y. Park, "Effects of copper addition on the formation of inclusions and the resistance to pitting corrosion of high performance duplex stainless steels," *Corrosion Science*, **53**, 1408–1416 (2011).
24. J. Zhang and D. J. Young, "Effect of copper on metal dusting of austenitic stainless steels," *Corrosion Science*, **49**, 1450–1467 (2007).
25. I. M. Fedorchenko and L. I. Pugina, *Composite Sintered Antifriction Materials* [in Russian], Naukova Dumka, Kiev (1980).
26. B. G. Hasanov, A. A. Azarenkov, Ye. V. Kharchenko, A. V. Skorikov, and Ye. R. Makhmudova, "Effect of the specific load on tribotechnical properties of powder iron-copper-graphite alloy impregnated with lubricant with an addition of a surfactant," *Izvestia Vysshykh Uchebnykh Zavedeniy, Severo-Kavkazskii Region, Tekhnicheskiiye Nauki*, No. 4 (200), 79–84 (2018).
27. B. G. Gasanov, A. A. Azarenkov, Zh. V. Kravchenko, and Ye. V. Kharchenko, "The mechanism of formation of secondary structure layers in the friction pair "powder iron-copper alloy — steel," in: *Problems of Triboelectrochemistry, Proceedings of the Int. Science and Technology Conf.*, Novocherkassk (2006), pp. 38–44.
28. P. A. Vityaz et al., *Powder Materials based on Iron and Copper. Atlas of Structures* [in Russian], Belarus, Nauka, Minsk (2008).
29. W. Aperador, J. Bautista-Ruiz, and J. Caicedo, "Wear synergy of copper-iron mixtures processed by powder metallurgy," *Rasayan Journal of Chemistry*, Special Issue, 193–199 (2021); <http://doi.org/10.31788/RJC.2021.1456678>.
30. N. V. Stepanova, A. A. Bataev, A. A. Sitnikov, and T. N. Oskolkova, "Wear resistance of eutectoid steel alloyed with copper and aluminum," *Obrabotka Metallov: Tekhnologiya, Oborudovaniye, Instrumenty*, No. 4 (69), 72–79 (2015).
31. L. Chen, Z. Zhang, Y. Huang, J. Cui, Z. Deng, H. Zou, and K. Chang, "Thermodynamic description of the Fe–Cu–C system," *Calphad: Computer Coupling of Phase Diagrams and Thermochemistry*, **64**, 225–235 (2019).
32. L. L. Oden and N. A. Gokcen, "Cu–C and Al–Cu–C phase diagrams and thermodynamic properties of C in the alloys from 1550 °C to 2300 °C," *Metallurgical Transactions B*, **23**, 4, 453–458 (1992); DOI: 10.1007/BF02649664.
33. H. Okamoto, "Supplemental literature review of binary phase diagrams: Ag–Cl, Br–Pb, Br–Zn, C–Cu, Ce–Zr, Cl–Zn, Fe–Lu, Fe–Tm, Ga–V, Nd–Ti, Nd–Zr, and Si–Ta," *J. of Phase Equilibria and Diffusion*, **37**, 2, 246–257 (2016); DOI: 10.1007/s11669-015-0433-z.
34. N. P. Lyakishev, *Phase Diagrams of the Metal Systems: Reference Book*, in 3 vol.: Vol. 1 [in Russian], ed. by N. P. Lyakishev, Mashinostroyeniye, Moscow (1996).
35. D. V. Lazurenko, G. I. Alferova, K. I. Emurlaev, Y. Y. Emurlaeva, et al., "Formation of wear-resistant copper-bearing layers on the surfaces of steel substrates by non-vacuum electron beam acladding using powder mixtures," *Surface and Coatings Technology*, **395**, Art. 125927 (2020).
36. G. W. Zhang, Y. Y. Kang, M. J. Wang, H. Xu, and H. M. Jia, "Atomic diffusion behavior and diffusion mechanism in Fe–Cu bi-metal casting process studied by molecular dynamics simulation and experiment," *Materials Research Express*, **7**, No. 096519 (2020).
37. K. Chen, X. Chen, Z. Wang, and H. M. R. Sandstrom, "Optimization of deformation properties in as-cast copper by microstructural engineering. Part I. Microstructure," *J. of Alloys and Compounds*, **763**, 592–605 (2018).
38. A. P. Pravarskii, "Study of the Fe–Cu–Al system," *Izv. AN SSSR, Metally*, No. 4, 220–222 (1971).